Journal of Luminescence 257 (2023) 119662

Contents lists available at ScienceDirect

Journal of Luminescence

journal homepage: www.elsevier.com/locate/jlumin

Full Length Article

The role of capping agents on the trapping levels structure and luminescent emission of $SrMoO_4$ phosphors

Ana Paula de Azevedo Marques [a], Nancy Kuniko Umisedo [b], Jessica Araujo Costa [a], Elizabeth Mateus Yoshimura [b], Emico Okuno [b], Roseli Künzel [c,*]

[a] Universidade Federal de São Paulo - UNIFESP, Departamento de Química, R. São Nicolau, 210 - Centro, Diadema, SP, CEP 09913-030, Brazil
[b] Universidade de Sao Paulo, Instituto de Física, Cidade Universitária, CEP 05508-900, Sao Paulo, SP, Brazil
[c] Universidade Federal de São Paulo - UNIFESP, Departamento de Fisica, R. Sao Nicolau, 210 - Centro, Diadema, SP, CEP 09913-030, Brazil

ARTICLE INFO

Keywords:
Ceramics
Luminescence
Microwave
Thermoluminescence
Traps levels

ABSTRACT

In the present work, we investigate the thermoluminescence (TL) and optically stimulated luminescence (OSL) from strontium molybdate $SrMoO_4$ powders designed with different capping agents. The samples were prepared through co-precipitation and processed in a Microwave-Assisted Hydrothermal (MAH) system. The structural, optical, and morphological characteristics were investigated using Raman, Fourier transform infrared spectroscopy (FTIR), DRX, ultraviolet-visible (UV–Vis) absorption, and Scanning electron microscopy (SEM). The TL glow curves recorded from as-prepared and irradiated samples with beta particles reveal that their intensity and profile depend on the used capping agent. The trapping depth energy, determined from the TL glows curves, ranges from 1.02 to 2.23 eV for the as-prepared samples and from 0.9 to 2.33 eV for the irradiated phosphors. The residual TL spectra, registered from successive readouts, indicate that the thermal treatment shifts the glow curve to lower temperatures suggesting the formation of shallower trap states. The outcomes reveal that the OSL signal and its behaviors with the radiation dose depend on the employed capping agent. The results show the TL and OSL signal's dependence on the structural properties and support the potential application of $SrMoO_4$ powders as an OSL detector.

1. Introduction

Strontium molybdate ($SrMoO_4$) belongs to the class of alkaline earth metal molybdates with a general formula $AMoO_4$, where A corresponds to the divalent cations (*i.e.* Ca^{2+}, Ba^{2+}, Sr^{2+}), and exhibits, at room temperature, a scheelite-type tetragonal structure and a space group of ($I_{41/a}$) [1]. This material has become the subject of intensive interest owing to its outstanding structural and optical properties, allowing their potential technological applications as catalysts, photocatalysts, laser materials, storage phosphors, gas sensors, scintillators, and radiation detectors [1–9].

Several methodologies are adopted to synthesize $SrMoO_4$ phosphors, including the Czochralski Method [10,11], co-precipitation [12–14], Conventional Solid-State Reaction Method [15,7], combustion syntheses [16,17], sol-gel [9], hydrothermal [18,19], sonochemical method [20], and microwave-hydrothermal [21–23,5], and others. The microwave-assisted hydrothermal method is excellent for preparing ceramic oxides with controlled morphology. It was reported that $SrMoO_4$ synthesized through the hydrothermal method displays some intrinsic defects that induce additional absorption bands, which profoundly affect their optical features and enhance their sensing properties [21]. The observed intrinsic defects are attributed to oxygen vacancies, interstitial Sr and interstitial oxygen in the $SrMoO_4$ lattice structure [21,4,24,25]. $SrMoO_4$ displays remarkable optical properties, with the main emission occurring in the green and blue spectral regions, and is recognized as a type of self-activated luminescent material [26,27]. An alternative experimental strategy employed to modify the organization level and tune the optical properties of materials is the use of capping agents. Using suitable capping agents can reduce particle agglomeration, and induce modifications in the disorder-order degree, particle morphology, and crystallite size [21]. Although the structural, optical, and morphological properties are extensively studied, to our present knowledge, the impact of the capping agents in the $SrMoO_4$ trapping parameters and their role in the density and distribution of structural defect states

---

* Corresponding author.
E-mail address: kunzel.roseli@unifesp.br (R. Künzel).

https://doi.org/10.1016/j.jlumin.2022.119662
Received 18 October 2022; Received in revised form 14 December 2022; Accepted 29 December 2022

remains unknown. In order to understand how the capping agents affect the location and distribution of the structural defects inside the bandgap, thermoluminescence (TL) and Optically Stimulated Luminescence (OSL) techniques can be employed for a careful investigation.

Molybdates, especially $SrMoO_4$, $CaMoO_4$, Li_2MoO_4, $PbMoO_4$ are studied as potential cryogenic scintillating material to be employed to investigate uncommon events in high energy physics [28–32]. Under X-ray excitation, the $SrMoO_4$ crystals, produced by the Czochralski method, exhibit a broad luminescence band in the 400 – 700 nm, peaking around 515 nm [33,34,29]. The energy efficiency of $SrMoO_4$ is around 6% of that observed for the CsI:Tl standard detector [29]. The relative defect concentration and their depth in the band gap may affect the scintillation yield, the optical, electrical, and magnetical properties [35,31,36–38]. These defects generate localized levels in the bandgap that act as carrier traps, affecting the kinetics of charge trapping and causing the TL and OSL emissions [39,40]. Thermoluminescence from undoped molybdates, including Li_2MoO_4, $BaMoO_4$, $SrMoO_4$, and $CaMoO_4$, suggests that the glow curves result from intrinsic defects and its profile and intensity depends on the adopted synthesis methodology [5,31,41,42]. The $SrMoO_4$ compounds were also investigated concerning their OSL emission. $SrMoO_4$ designed by co-precipitation and submitted to a hydrothermal treatment revealed that $SrMoO_4$ is a promising material to be applied as an OSL radiation sensor under beta particle irradiation [5]. The results showed that the OSL signal appears after thermal annealing, which induces the formation of shallower trapping states responsible for the OSL emission. On the other hand, the OSL emission from $SrMoO_4$, also designed by co-precipitation without hydrothermal treatment, does not present a linear OSL response with the beta particle dose. Therefore, these recent results suggested that the trapping depth, defects density, and distribution affect the $SrMoO_4$ OSL response [5].

In the present work, we investigate the TL and OSL response in $SrMoO_4$ phosphors prepared by co-precipitation followed by the microwave-assisted hydrothermal method using four different capping reagents. The main goal of this work is to determine the kinetic parameters of the trapping structure from TL glow curves $SrMoO_4$ phosphors using computational and well-established empirical methods published in the literature. The morphological, structural, and optical properties are evaluated in full detail. The OSL response over a wide dose interval was investigated for the designed materials.

2. Materials and methods

The $SrMoO_4$ powders were prepared by co-precipitation and processed by the microwave-hydrothermal technique using four types of surfactants. The employed chemical reagents were as follows: molybdenum trioxide (MoO_3) (Alfa Aesar, 99.95%), strontium acetate ($(CH_3CO_2)_2Sr)$) (Alfa Aesar, 99%), citric acid ($H_3C_6H_5O_7$) (Mallinckrodt, 99%). The used surfactants were from Sigma-Aldrich (99.9%) named as follows: polyethylene glycol ($HOCH_2CH_2OH$), Mw 200 - PEG 200, Mw 400 - PEG 400, Mw 600 - PEG 600, and CTAB (N-cetyltrimethylammonium bromide) with 364.45 g/mol Mw [21]. As described in previous works, the samples were synthesized using the co-precipitation method followed by microwave-assisted hydrothermal treatment (MAH) [21]. The synthesis procedure follows: Under vigorous stirring 5×10^{-3} mol of MoO_3 was dissolved in around 50 mL of distilled water. Following 5×10^{-3} mL of $(CH_3CO_2)_2Sr$ and surfactant was added under constant stirring. The pH of the solution was adjusted to 12, adding KOH. The samples were then submitted to an additional MAH treatment at 100 ^oC for 16 min. The resulting white precipitate was collected, washed with ethanol and water, and dried at 60 ^oC. Raman spectra were registered using a Renishaw microscope (in Via model) with a multichannel CCD detector and He-Ne laser (632.8 nm) from 80 cm^{-1} to 1000 cm^{-1}, with the automatic cosmic ray removal option set on. The Fourier Transformed Infrared spectra (FTIR) were registered with a Shimadzu IRPrestige-21 spectrophotometer in the spectral range from 500 to 1000 cm^{-1}. The absorbance measurements were performed on a Shimadzu UV-2600 spectrophotometer in the wavelength range from 200 to 800 nm and a spectral resolution of 0.1 nm. In wavelength units, the UV-Vis absorbance spectra were converted to energy scale using the Jacobian Conversion method [43]. The band gap energy was calculated employing the Tauc relation [44,45]. The particle morphology was observed using a scanning electron microscope, SEM (Jeol JSM-6610LV). The DRX measurements were performed using a DRX D8 ADVANCE equipment (Bruker) using Cu-Kα radiation ($\lambda = 1.5418$ Å), in the 2θ range from 15^o to 75^o with increment of 0.02^o/min.

The thermoluminescence (TL) and Optically Stimulated Luminescence (OSL) signals were recorded employing a Risø TL/OSL reader, model DA-20, with a built-in $^{90}Sr/^{90}Y$ beta source, 1.48 GBq activity. The dose rate supplied to the samples is about 10 mGy/s [46]. The $SrMoO_4$ powders, three aliquots with about 6 mg each, were exposed to a 1.2 Gy beta radiation dose. The thermal stimulation in this device is provided by a heating component that increases the temperature linearly. In this work, the adopted heating rates were 3 K/s and 5 K/s. The TL measurements were performed using two optical filters: (a) a Hoya U-340, with 7.5 mm thickness and transmission window from 270 nm to 380 nm, and (b) a blue filter pack with a transmission window from 320 nm to 450 nm. The background signal was evaluated by measuring the TL signal from an empty sample holder. The OSL measurements were carried out using a blue LED array light source with emission at 470 nm to provide optical stimulation and the Hoya U-340 optical filter. The OSL data were registered for excitation times ranging from 1 to 60 seconds, in continuous wave mode, with a radiance of 80 mW/cm^2. The samples were subjected to successive TL and OSL readouts to evaluate the effect of heating treatments on the registered signal. The OSL signal was also registered in the dose range from 0.8 Gy to 10 Gy.

2.1. TL glow curve deconvolution

The experimental glow curves were analyzed adopting the computadorized curve deconvolution analysis (CCDA) based on the single glow-peak equation of general order kinetics [47]:

$$I(T) = I_m b^{\frac{b}{b-1}} exp\left(\frac{E}{kT}\frac{T-T_m}{T_m}\right) \times \left[(b-1)(1-\Delta)\frac{T^2}{T_m^2} exp\left(\frac{E}{kT}\frac{T-T_m}{T_m}\right) + Z_m\right]^{\frac{-b}{b-1}} \quad (1)$$

where $\Delta = \frac{2kT}{E}$, $\Delta_m = \frac{2kT_m}{E}$ and $Z_m = 1 + (b-1)\Delta_m$

E is to the trap depth, b, the order of the kinetics, T_m, the temperature of the maximum intensity of the peak, and k, the Boltzmann's constant. The glow curve deconvolution was performed with the Microsoft Excel software, employing the Solver utility [48].

The frequency factor (s) is estimated using the following equation [47]:

$$s = \frac{\beta E}{kT_m^2}\frac{1}{Z_m} exp\left(\frac{E}{kT_m}\right) \quad (2)$$

The goodness of fit was determined by computing the Figure of Merit (FOM) [49]:

$$FOM = \frac{\sum_p |TL_{exp} - TL_{fit}|}{\sum_p TL_{fit}} \quad (3)$$

where TL_{exp} are the experimental data and TL_{fit} the adjusted data.

The charge carriers expected lifetime (τ) in each trapping level for $SrMoO_4$ samples, at room temperature ($T = 300$ K), was evaluated from the equation [50]:

$$\tau = s^{-1} exp\left(\frac{E}{kT}\right) \quad (4)$$

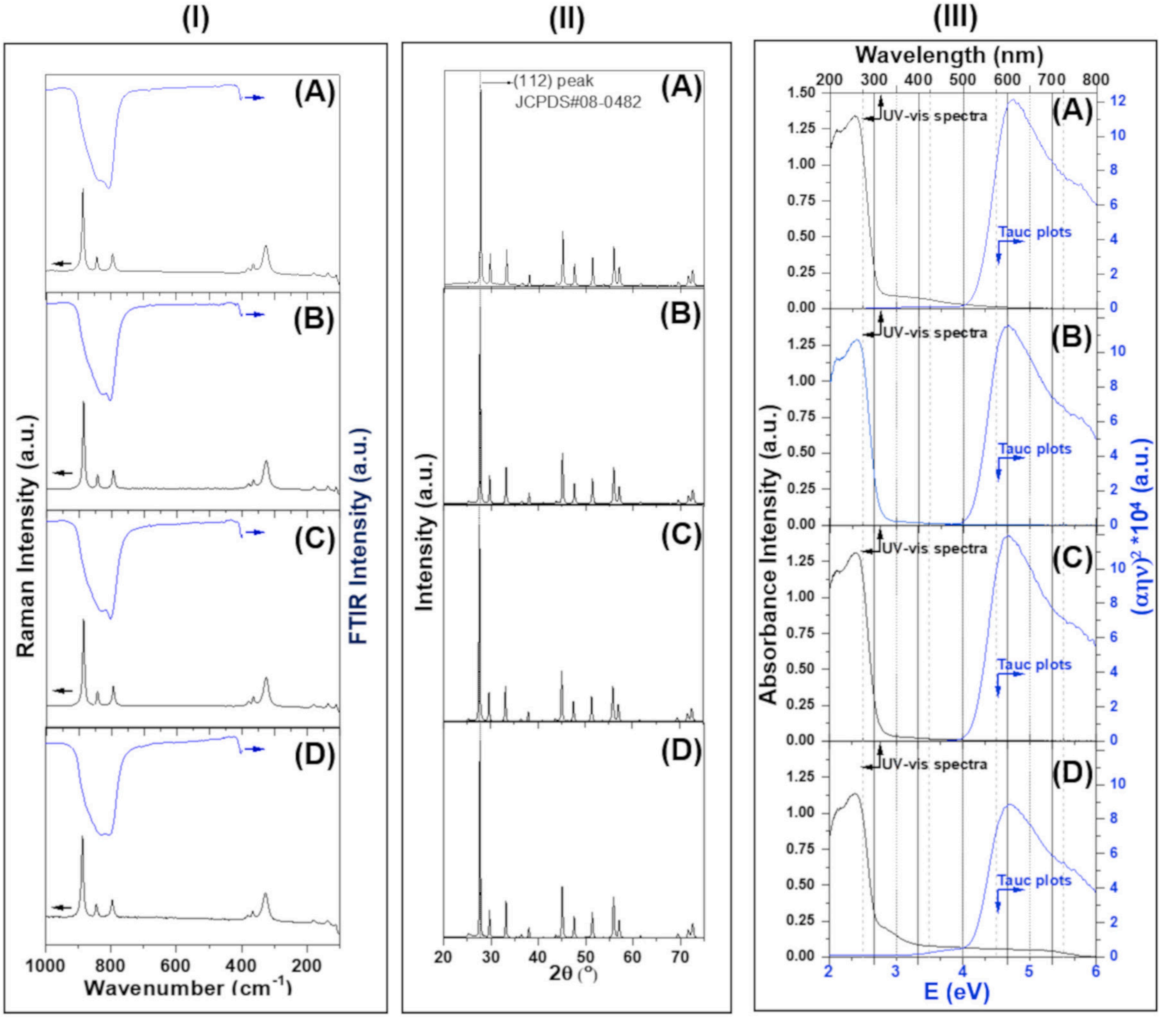

Fig. 1. FTIR, Raman, DRX, UV-Vis measurements and Tauc plot for (A) PEG200, (B) PEG400, (C) PEG600, and (D) CTAB SMO samples produced by co-precipitation followed by microwave hydrothermal treatment.

The expected trapping level lifetime corresponds to the time required for the TL peak intensity to be reduced by a factor $1/e$ of its initial value [51].

3. Results and discussion

3.1. Structural and optical properties

Fig. 1 (A-D(I)) shows the registered FTIR and Raman spectra from the $SrMoO_4$ samples, designed by co-precipitation and processed in a microwave-hydrothermal, using different capping agents as described before (PEG200, PEG400, PEG600, and CTAB). The SMO powders have tetrahedral symmetry (T_d), with the $F_2(\nu_3)$ (antisymmetric stretch) and $F_2(\nu_4)$ (bending modes) vibrations infrared active [21]. The registered FTIR spectra exhibit a broad band between 750 and 950 cm^{-1}. These bands are assigned to $F_2(\nu_3)$ and are related to the Mo-O antisymmetric stretch vibration in MoO_4^{2-} tetrahedra.

The Raman spectra of molybdates exhibit internal and external vibrational modes [22,21]. The internal vibration modes are connected to the tetrahedral $[MO_4]^{2-}$ cluster vibration in the lattice with a stationary mass center [21]. These vibrations comprise three stretches ($A_g + B_g + E_g$) and four modes identified as $\nu_1(A_1)$, $\nu_2(E)$, $\nu_3(F_2)$, and $\nu_4(F_2)$ [10,12]. The internal vibrational Raman modes in the studied samples are located around 886 cm^{-1} (ν_1(Ag)), 845 cm^{-1} (ν_3(Bg)), 796 cm^{-1} (ν_3(Eg)), 382 cm^{-1} (ν_4(Eg)), 367 cm^{-1} (ν_4(Bg)) and 328 cm^{-1} (ν_2(Bg)); and, all these Raman modes are assigned to the tetrahedral $[MO_4]^{2-}$ cluster vibration in the lattice with a stationary mass center. The peak at 182 cm^{-1} corresponds to the free rotation. The observed bands in the range from 97–140 cm^{-1} are the external vibrational modes and are associated with the motion of the rigid molecular unit and the Sr^{2+} cations [22,21]. No additional peaks are observed in the Raman spectra indicating no additional phase. These results agree with that reported in the literature for $SrMoO_4$ structures [21].

We calculated the Raman line-shape asymmetric broadening from the experimental data for the peak centered around 885 cm^{-1}. The asymmetric ratio is defined as $AR = \Gamma_L/\Gamma_H$ where Γ_L and Γ_H correspond to the half widths on the left (lower frequency) and right (high frequency) side, respectively, relative to the center of the peak [52]. The asymmetric factors calculated are $AR = 0.93$ (PEG200), 1.03 (PEG400), 0.99 (PEG600), and 0.97 (CTAB). Asymmetric factors lower than 1.0 indicate that the peak has a broader half-width (Γ_H) on the higher-frequency side of the peak position. The asymmetric ratio changes among the samples reveal that the studied powders present different levels of disorder degrees.

The structure of the as-prepared $SrMoO_4$ powders and phase purity were confirmed by the X-ray diffraction (XRD) technique, and the registered patterns are displayed in Fig. 1(A-D(II)). The utilization of different capping agents impacts particle growth and agglomeration, influencing the structural properties [53]. The registered diffraction peaks can be indexed for a scheelite-type tetragonal structure with space group I41/a (JCPDS card No 85-0586). The sharp and intense peaks reveal that the prepared powders are well crystallized. The diffrac-

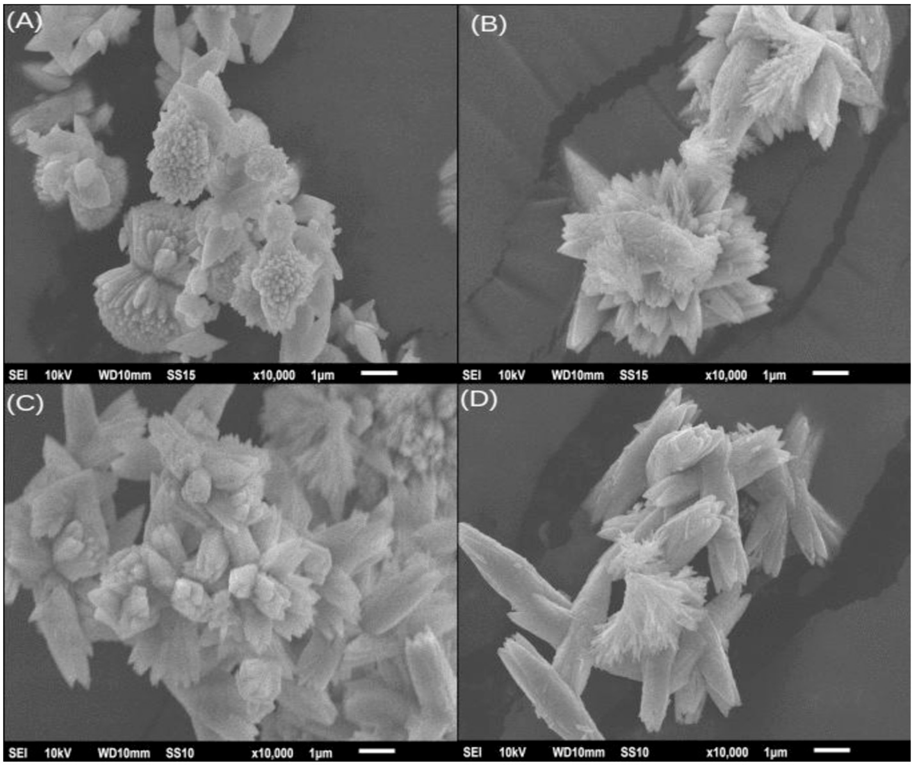

Fig. 2. SEM micrographs of the hydrothermal synthesized $SrMoO_4$ with different capping agents (A) PEG200, (B) PEG400, (C) PEG600 and (D) CTAB at 10000x.

tion peak (112) occurs around $2\theta = 27.68^o$ (PEG200), 27.69^o (PEG400), 27.61^o (PEG600), and 27.66^o (CTAB), revealing the formation of crystalline scheelite-type phase. From the JCPDS card No. 08-0482, this peak with 100% intensity occurs at $2\theta = 27.66^o$, indicating that the experimental data agree with the standard one, with a slight variation on the peak position. The full widths at half maximum (FWHM) for the (112) plane are FWHM = 0.247 (PEG200), 0.257 (PEG400), 0.265 (PEG600), and 0.243 (CTAB). The discrete variations in the XRD peak positions and FWHM values can be attributed to the different densities of defect concentrations in the samples. High defect concentration in materials impacts their internal strain field, changing their XRD profiles compared to moderately defect-free powders [54]. Higher defect concentrations broaden the full widths at half maximum (FWHM) and induce XRD peak shifting [55,56]. As observed by Paradelas et al. [21], the modifications on the diffraction angles affect the lattice parameters and the crystallite size and are induced by defects. The crystal structure's distortions can be related to intrinsic defects such as interstitial strontium ions, oxygen vacancy, interstitial oxygen ions, and defect clusters. In particular, the Frenkel defects (oxygen vacancy and interstitial oxygen) are recognized as the dominant defect type in $CaWO_4$ materials due to the lower formation energy [57,58]. Therefore, considering that the samples investigated in this work have a similar crystalline structure to $CaWO_4$, the defects in the $SrMoO_4$ powders could also be associated with the Frenkel defects [38].

Fig. 1 (Fig. 1(A-D(III)) shows the absorbance spectral dependence and the Tauc plot for the $SrMoO_4$ samples. The absorbance spectra obtained, in wavelength units, were converted into energy units using the Jacobian conversion method [43]. The absorption spectra display broadband with the maximum intensity in the ultraviolet region from 300 nm (4.13 eV) to 200 nm (6.2 eV), assigned to the electronic transitions of the $[MoO_4]^{2-}$ complex. To calculate the optical bandgap, considering directly allowed transitions [21], the equation proposed by Wood and Tauc was used [45]. The calculated band gap values for the samples are 4.16 (±0.03) eV for the sample designed with PEG200, 4.10 (±0.01) eV for PEG400, 4.11 (±0.01) eV for PEG600 and 4.06 (±0.01) eV for CTAB. The determined band gap values agree with those published in the literature for $SrMoO_4$ compounds [20]. The optical absorption profile and bandgap values depend on the degree of structural order-disorder in the lattice structure [59]. More ordered structures exhibit higher gap energy than those observed for lower ordered materials because the defects induce intermediate energy levels within the bandgap, reducing the gap energy value [60]. In our study, the UV–vis spectra evidenced changes in band gap energies for the samples designed with different capping agents, indicating different order-disorder degrees. Therefore, the results show an increase in structural disorder of $SrMoO_4$ synthesized in the presence of CTAB observed as a reduction of the bandgap energy, compared with the sample prepared with PEG200.

3.2. *Morphological properties*

Micrographs of $SrMoO_4$ samples display octahedral morphologies, as expected, and the images show that the particles agglomerate and form different arrangements (Fig. 2 (A-D)). The shape and size of the formed structures depend on the used capping reagent. It is observed in Fig. 2 (A) that the use of PEG200 results in increased structures while the agglomeration degree decreases for the samples designed by employing capping agents with an increased molecular chain (Fig. 2 (B-D)). Therefore, as observed by Paradelas et al. (2017), different capping reagents deeply affect the crystal growth process and result in different particles size and defect levels [21].

3.3. *Thermoluminescence and optically stimulated luminescence*

Thermoluminescence glow curves were measured to study the trap level structure and the influence of the different capping agents on the trapping parameters. Fig. 3(A) shows the glow curves, registered using the blue filter pack at 3 K/s heating rate, from as-prepared samples. The results show that maximum TL emission and the glow curve profile change according to the used capping agent for both as-prepared and irradiated samples, indicating that the used capping reagent affects the trap depth levels structure of the samples in agreement with the results from structural analysis. The samples display broad glow

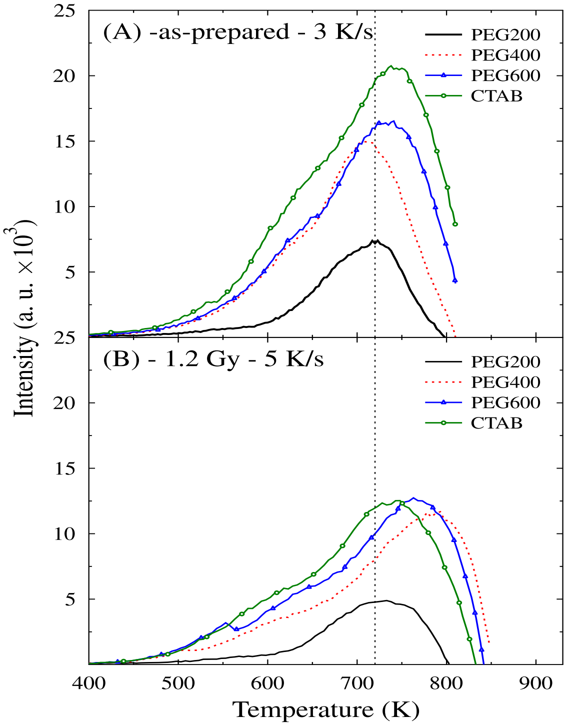

Fig. 3. Thermoluminescent glow curves from SMO samples produced using PEG200, PEG400, PEG600 and CTAB capping agents measured from (A) as-prepared at 3 K/s and (B) irradiated with 1.2 Gy at 5 K/s heating rate. The vertical dashed line corresponds to the peak of the as-received PEG200 sample.

curves ranging over an extensive temperature range. The SMO-PEG200 sample depicts a narrower and lower intensity glow curve peaking at around 720 K. The glow curves from SMO-PEG400, SMO-PEG600, and SMO-CTAB peaks at 711 K, 737 K, and 743 K, respectively. The most intense and broader glow curve is observed for the SMO-CTAB sample. Fig. 3(B) shows the registered glow curves at 5 K/s for the irradiated samples with 1.2 Gy beta radiation. The maximum emission for the SMO-PEG200, SMO-PEG400, SMO-PEG600, and SMO-CTAB samples is 731 K, 786 K, 763 K, and 741 K, respectively. The TL signal for the SMO-PEG200 sample is lower than the intensity registered for the other samples, suggesting a lower trap density or even a lower concentration of recombination centers, or the emitted wavelength has a lower detection efficiency. Additionally, the lower intensity of the TL glow curve can also indicate a higher distance between traps and recombination centers, reducing the light emission efficiency [5]. The comparison of Fig. 3 A and B shows the modifications induced in the material structure as a result of the irradiation with beta particles; it is possible to observe that the glow curves of some materials shift to the lower temperature side (SMO-CTAB) while others shift to the higher temperature side. Although the use of higher heating rates shifts the glow curves to the higher temperature side, it is evident from the Fig. 3 the occurrence of variation on the peak position, and intensity, for irradiated samples compared to its as-prepared counterpart.

The glow curve deconvolution method was adopted to calculate the trapping parameters for the as-prepared and irradiated samples. The number of peaks required to deconvolve each spectrum was defined by calculating the second derivative of the glow curve spectra measured for each sample. The glow peak of the as-prepared SMO-PEG200 sample was fitted with four peaks, and the glow curves of all the other samples required five peaks. For the irradiated samples, all the glow curves were adjusted with five peaks (Fig. 4(A-D)). After defining the number of peaks for each spectrum, the parameters for each glow curve were computed based on the general kinetics approximation. The trapping depth, frequency factor, and maximum temperature are calculated for each peak from the best fit of the deconvolved spectra to the experimental data. Table 1 brings the calculated TL kinetic parameters and the trapping level time for each peak. The FOM (Figure Of Merit) values for all samples are lower than 3.0% revealing an excellent fitting to the experimental data.

The determined activation energy (E_p), or trap depth, are in the range of 0.93 eV to 2.19 eV for the as-prepared samples and from 0.90 eV to 2.33 eV for the irradiated powders (Table 1). The results show that the irradiation with beta particles, with 1.2 Gy, reduces the activation energy for the first peak for all the studied samples. However, the higher decrease for the peak 1 from the deconvolved spectra was observed for the PEG200 (22% decrease) and PEG400 (12%) samples. The frequency factor values, related to the thermal release of electrons from traps, range from 1.6×10^8 s^{-1} to 8.3×10^{13} s^{-1} for the as-prepared samples. For irradiated powders, the frequency factor ranges from 1.2×10^8 s^{-1} to 9.9×10^{13} s^{-1}. The determined values of s are within the physically acceptable range from 10^8 to 10^{14} s^{-1} [50]. Results show a subtle variation in the activation energy for the samples submitted to beta particle irradiation, with the determined values spanning over a broader range than their as-prepared samples counterpart. Additionally, the trapping depth energy of the irradiated SMO-PEG400 for the whole curve shifts to lower energies. The determined trapping lifetime, at 300 K, is shown in Table 1. The trapping lifetime ranges from 221 days to 6.1×10^{15} years for the as-received samples. For the irradiated powders, the trapping level time ranges from 43 days to 4.5×10^{17} years. The outcomes indicate an increase in the trapping level lifetime values with the increase of the trapping depth energy. The observed Shift of the trapping depth energy to lower values for the first TL peak, induced by the beta particle irradiation, also affects the trapping level lifetime. These results suggest that irradiating the $SrMoO_4$ powders may produce radiation-induced point defects, defects clusters, and more complicated defect structures affecting the TL glow curve profile and intensity [42,61].

The effect of the thermal treatment on the glow curves profile was investigated by executing a series of successive TL readouts at 3 K/s until 873 K employing the same sample using the blue filter pack (Fig. 5(A-D)). The experimental procedure is illustrated in Fig. 6 according to the following steps: (I) TL readout (TL1); (II) TL reading (TL2), (III) Irradiation with β particles (irradiation-1); (IV) TL reading (TL3); (V) TL reading (TL4); (VI) Irradiation with β particles (irradiation-2); (VII) TL reading (TL5) and (VIII) TL reading (TL6).

The black curve for each group (PEG200-TL1, PEG400-TL1, PEG600-TL1, and CTAB-TL1) corresponds to the glow curve registered from as-prepared powders submitted to a heating rate of 3 K/s in the temperature range from 300 K to 873 K (Fig. 5). The other curves correspond to consecutive readouts performed with the same sample. The red color curves correspond to the luminescent emission from the same sample submitted to the previous TL1 readout without any additional treatment or irradiation (PEG200-TL2, PEG400-TL2, PEG600-TL2, and CTAB-TL2). Results show that the luminescence emission did not disappear after the first readout (TL1), and the glow curves registered on the second readout (TL2) show that the peak shifts to lower temperatures for all the samples. The observed luminescence indicates modifications in the material trapping structure with the appearance of shallower trapping states due to the heating treatment. After this, the sample was irradiated with beta particles (irradiation-1) and submitted to a subsequent TL readout assigned as TL3 in Fig. 5. The luminescence was registered for more one TL readout (TL4), and the last TLs readout (TL5 and TL6) were preceded by irradiation with a 1.2 Gy dose from beta particles (irradiation-2). The results show that the luminescence curve gets broader after the first TL readout, and the glow curves shift to lower temperatures. The glow curve profile is not affected by the subsequent TL readouts and irradiation. However, the intensity of the glow curves decreases even with further irradiation.

The effect of different capping agents in the defect structure in $SrMoO_4$ powders was also investigated through Optically Stimulated Luminescence (OSL) measurements. The experimental cyclic procedure

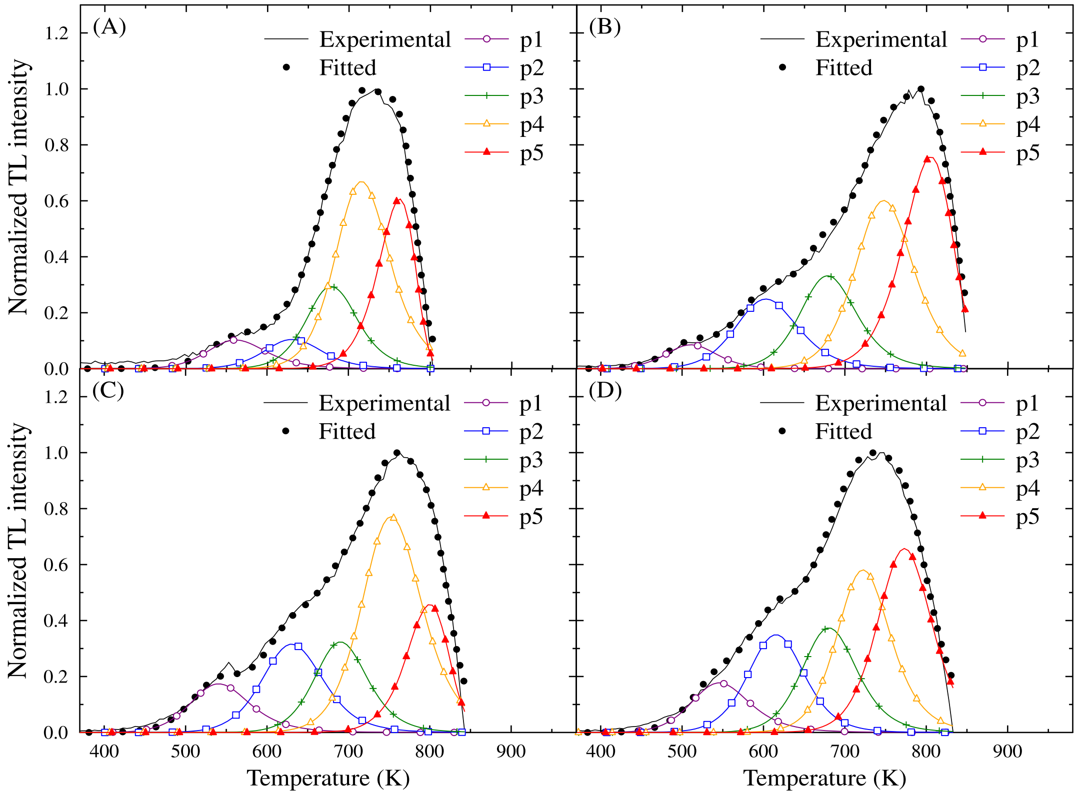

Fig. 4. Deconvolution of experimental TL glow curves measured at 5 K/s heating rate from $SrMoO_4$ samples designed with (A) PEG200, (B) PEG400, (C) PEG600 and (D) CTAB exposed to 1.2 Gy beta radiation.

Table 1
Kinetic parameters and lifetime of charge in trap (τ) of the deconvoluted thermoluminescent peaks measured for the as prepared and irradiated $SrMoO_4$ samples designed with different surfactants (PEG 200, PEG 400, PEG 600, and CTAB). The heating rate is 3 K/s (for the as-prepared) and 5 K/s for the irradiated samples. The b values show a clear trend towards second order kinetics for all the samples.

$SrMoO_4$ Sample/ Peak	as-prepared (3K/s)				1.2 Gy (5 K/s)			
	T_p (K)	E_p (eV)	Frequency factor (s^{-1})	τ (300 K)	T_p (K)	E_p (eV)	Frequency factor (s^{-1})	τ (300 K)
PEG200								
1	550	1.32	3.6×10^8	1.3×10^6 y	560	1.03	1.94×10^8	33.4 y
2	625	1.5	1.8×10^{11}	2.8×10^6 y	630	1.29	2.2×10^9	6.9×10^4 y
3	680	1.83	4.8×10^{12}	3.7×10^{10} y	678	1.51	8.95×10^{11}	8.4×10^5 y
4	732	1.98	5.4×10^{12}	1.1×10^{13} y	715	1.86	1.53×10^{12}	3.7×10^{11} y
5	–	–	–	–	762	2.21	4.69×10^{13}	9.2×10^{16} y
PEG400								
1	505	0.93	2.2×10^8	221 days	500	0.87	1.1×10^8	43 days
2	590	1.07	1.4×10^8	2.2×10^2 y	602	1.09	2.2×10^8	3.2×10^2 y
3	648	1.43	1.5×10^{10}	2.3×10^6 y	678	1.57	8.7×10^{10}	8.8×10^7 y
4	710	1.81	8.3×10^{11}	9.9×10^{10} y	747	1.85	5.5×10^{11}	7.1×10^{11} y
5	755	1.98	1.9×10^{12}	3.1×10^{13} y	805	1.94	2.4×10^{11}	5.2×10^{13} y
PEG600								
1	560	1.03	1.9×10^8	34 y	540	0.95	1.3×10^8	2.3 y
2	630	1.29	2.2×10^9	6.9×10^4 y	630	1.22	9.5×10^8	1.1×10^4 y
3	678	1.73	8.9×10^{11}	4.2×10^9 y	690	1.73	8.6×10^{11}	4.3×10^9 y
4	718	1.86	1.3×10^{12}	4.4×10^{11} y	752	1.85	4.5×10^{11}	8.6×10^{11} y
5	765	2.19	3.3×10^{13}	6.1×10^{15} y	800	2.33	9.9×10^{13}	4.5×10^{17} y
CTAB								
1	560	1.03	1.9×10^8	34 y	545	0.98	1.2×10^8	7.8 y
2	630	1.29	2.2×10^9	6.9×10^4 y	615	1.22	1.1×10^9	9.2×10^3 y
3	685	1.73	6.5×10^{11}	5.7×10^9 y	680	1.61	9.7×10^{10}	3.7×10^4 y
4	735	1.86	6.4×10^{11}	8.9×10^{11} y	722	1.91	2.6×10^{12}	1.5×10^{12} y
5	770	2.0	1.4×10^{12}	9.1×10^{13} y	773	2.08	4.2×10^{12}	6.7×10^{14} y

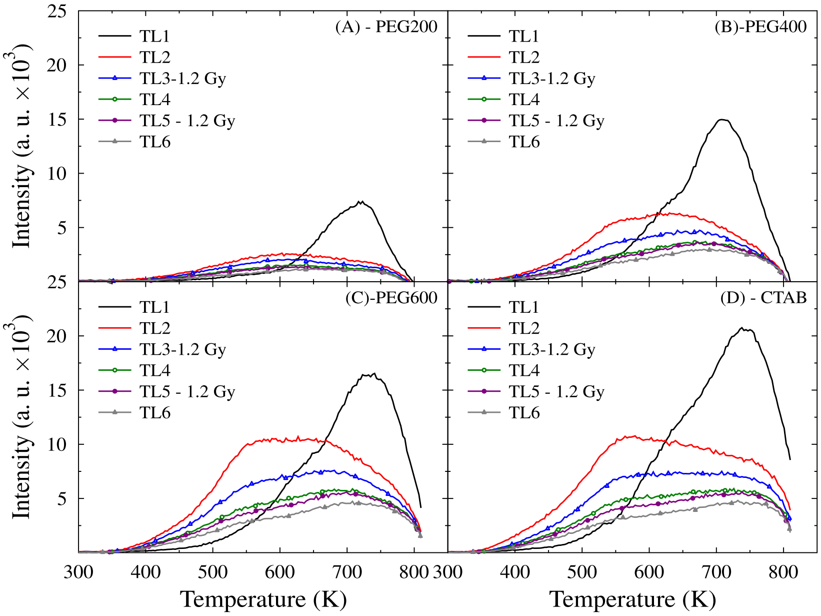

Fig. 5. Glow curves from $SrMoO_4$ samples submitted to several sequential TL readouts at 3 K/s for (A) PEG200, (B) PEG400, (C) PEG600 and (D) CTAB capping agents.

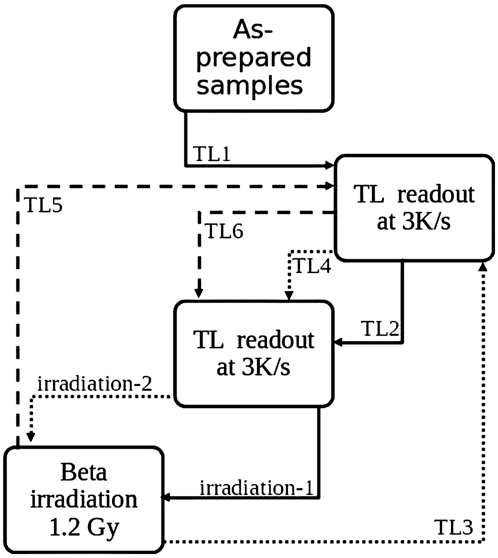

Fig. 6. Experimental procedure used in the successive TL measurements.

used in the OSL measurements is illustrated in Fig. 7. The measurements were performed using the Hoya U-340 filter.

The as-prepared samples were irradiated with a 4 Gy dose (Step 1 - irradiation-1) from beta particles and submitted to a first OSL readout (Step 2 - OSL1). After this, the samples were subjected to a TL readout at 3 K/s until 873 K (Step 3 - TL1), a CW-OSL readout (Step 4 -OSL2), and then subjected to subsequent irradiation with beta particles (Step 5 - irradiation-2) followed by a CW-OSL readout (Step 6 - OSL3). Steps 5 and 6 were repeated nine times in the dose range from 0.8 Gy to 10 Gy. Fig. 8 shows the OSL emission from the irradiated sample (Step 2), after the TL readout (Step 4), and after irradiation with 7.5 Gy (Step 6) for SMO-PEG200, SMO-PEG400, SMO-PEG600, and SMO-CTAB samples. The results show that no OSL signal was observed for the SMO-PEG200 sample under any conditions. For the SMO-PEG400 sample, the OSL emission appears for the irradiated sample without a previous thermal treatment (Step 2). Without a previous thermal treatment, the OSL signal is not observed for the irradiated SMO-PEG200, SMO-PEG600, and SMO-CTAB samples (Step 2). The OSL signal after a thermal treatment without additional irradiation (Step 4) seems to have a slower decay time for the PEG400, PEG600, and CTAB SMO samples. The SMO-PEG600 sample has no OSL signal in Step 2 (irradiated with 4 Gy) and after Step 6, where the sample received thermal treatment and irradiation with 7.5 Gy. The PEG400 SMO sample presents OSL emission in Steps 4 and 6. However, in Step 4 (after TL readout), the signal shows a slower decay than those registered after the irradiation with 7.5 Gy (Step 6), which decays very fast. These results suggest that the OSL signal, immediately after the TL measurement, has the contribution of charges trapped at deeper defect states that are not accessible to the optical stimulus. In this case, the heat provides the energy to promote these trapped charges at deeper levels to shallower defect states accessible to the optical stimulus, resulting in the slow decay OSL emission.

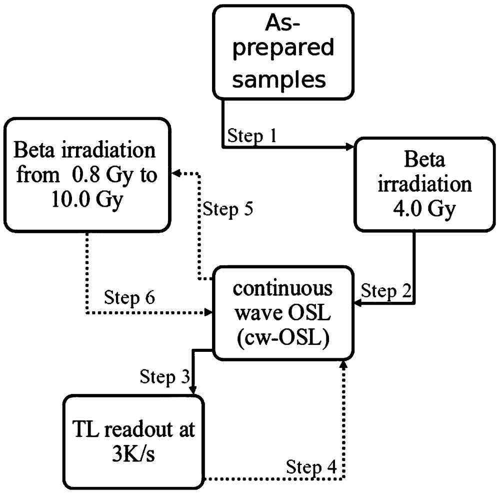

Fig. 7. Experimental procedure used in the successive OSL measurements.

Fig. 9 shows the increase of the OSL signal with the radiation dose, in the range between 0.8 Gy and 10 Gy for the PEG400 and CTAB samples. The OSL data were registered in steps of 0.3 seconds. Fig. 9(A) shows that the OSL signal decays quickly, before one second, for the

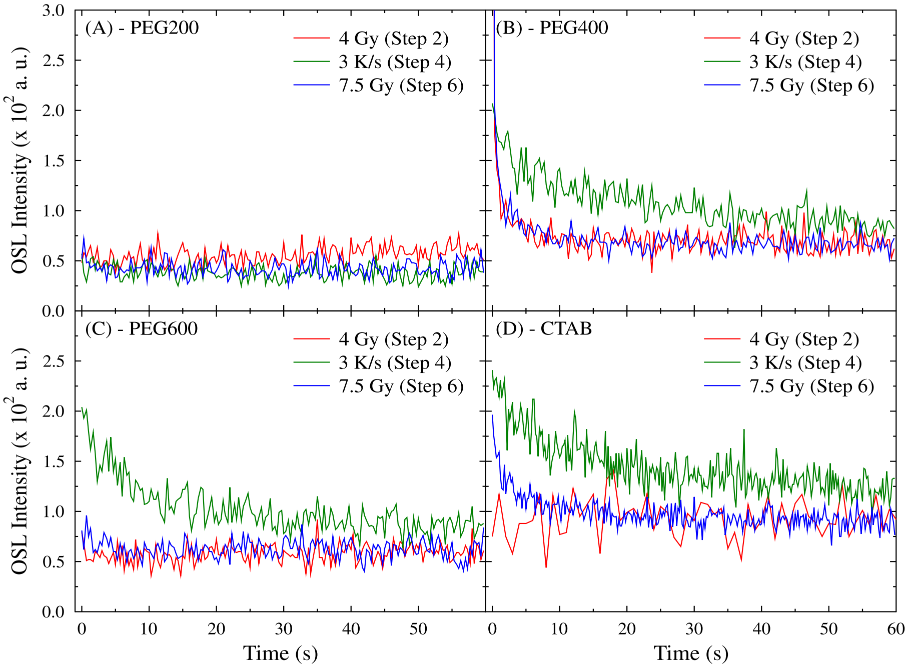

Fig. 8. OSL signal from irradiated $SrMoO_4$ samples (4 Gy) submitted to a thermal treatment (3 K/s) and subsequent irradiation (7.5 Gy) for (A) PEG200, (B) PEG400, (C) PEG600 and (D) CTAB capping agents.

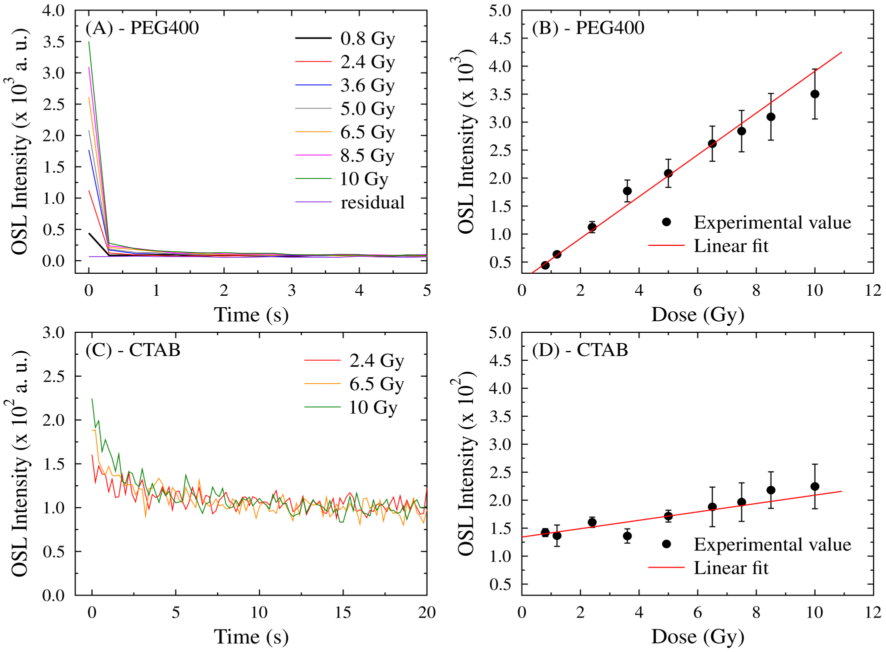

Fig. 9. OSL decay curves and dose response from $SrMoO_4$ samples submitted to a previous TL readouts at 3 K/s for powders designed using (A and B) PEG400, and (C and D) CTAB capping agents.

PEG400 sample, where the very fast OSL component entirely dominates the net signal. The intensity of the OSL signal grows linearly with the increase of the radiation dose (Fig. 9(B)). The OSL signal slightly increases with the applied radiation dose for the SMO-CTAB sample. However, the SMO-CTAB sample shows a slower decay time compared with the SMO-PEG400 samples (Fig. 9(C)) and a lower sensitivity with the radiation dose (Fig. 9(D)). For PEG400, the OSL signal disappears after 60 s illumination with blue light; that is, the exposure to 60 seconds under blue light was sufficient to empty the sample traps responsible for the OSL signal. The observed results show that using capping agents deeply affects the luminescence emission of $SrMoO_4$ phosphors and the signal decay time. The OSL signal is suppressed for the beta-irradiated PEG200 and PEG600 powders in the dose range from 0.8 Gy and 10 Gy. The comparison of the TL and OSL residual signals (Figs. 5 and 9), where the residual OSL is close to the background and the residual TL glow curve is observed shifted to lower temperatures, suggests that the traps responsible for TL are not responsible for OSL. However, this issue deserves further investigation. Finally, to the best of our knowledge, this is the first time that a kinetic study has been done for the thermoluminescence and optically stimulated luminescence from $SrMoO_4$ designed with different capping agents.

4. Conclusions

In this work, $SrMoO_4$ nanostructures were synthesized by co-precipitation, using different capping agents (PEG200, PEG400, PEG600, and CTAB), followed by microwave-assisted hydrothermal (MAH) treatment. The characterization techniques, XRD, Raman, and FTIR spectra, were used to identify the Scheelite-type structure of $SrMoO_4$ compounds and the distinct structural order-disorder degree as a consequence of the used capping agent. The octahedral morphology, with different levels of agglomeration of the designed powders, was observed by SEM microscopy. The calculated band-gap values range from 4.06 to 4.16 eV due to structural modifications and variations in intermediary energy levels within the band-gap. The TL glow curves showed a broad peak for all the as-prepared and irradiated samples, and the maximum emission temperature depends on the used capping agent. The trapping parameters, calculated through the deconvolution of the recorded glow curves, show that distinct capping agents and irradiation with beta particles affect the kinetic parameters due to the defect concentrations and distribution changes. The residual TL spectra, registered from successive readouts, reveal that the thermal treatment provokes the shift of the glow curve to lower temperatures when compared with the original TL peak indicating the formation of shallower trap states. The OSL signal for two irradiated samples, designed with PEG400 and CTAB capping agents, shows a linear variation of the luminescence intensity with the radiation dose ranging from 0.8 Gy to 10 Gy. The CW-OSL decay curves recorded for the powder designed with PEG400 decay quickly, before one second, and the fast OSL component entirely dominates the net signal. The results also reveal that the PEG400, PEG600, and CTAB samples exhibit a slow decay OSL emission after the TL readout suggesting that the thermal energy promotes electrons trapped at deep defect states to shallower traps accessible to the optical stimulation. This work's outcomes reinforce the OSL emission's dependence on the trapping structure and the potential application of $SrMoO_4$ powders as an OSL detector.

Declaration of competing interest

The authors declare that they have no known competing financial interests or personal relationships that could have appeared to influence the work reported in this paper.

Data availability

Data will be made available on request.

Acknowledgements

The authors are grateful to NIPE-Unifesp for experimental support and to Multiuser Equipment Center facilities of Unifesp Diadema (CEMUD-ICAQF/UNIFESP) for the XRD characterization technique. We also acknowledge the financial support from the Brazilian agencies Conselho Nacional de Desenvolvimento Científico e Tecnológico (CNPq) (Finance Code 576563/2008-0) and Sao Paulo Research Foundation (FAPESP) (#2016/20578-5, and #2013/07437-5).

References

[1] J. Rushbrooke, R. Ansorge, Optical fibre readout and performance of small scintillating crystals for a fine-grained gamma detector, Nucl. Instrum. Methods Phys. Res., Sect. A, Accel. Spectrom. Detect. Assoc. Equip. 280 (1) (1989) 83–90, https://doi.org/10.1016/0168-9002(89)91274-6.

[2] D. Errandonea, L. Gracia, R. Lacomba-Perales, A. Polian, J.C. Chervin, Compression of scheelite-type SrMoO4 under quasi-hydrostatic conditions: redefining the high-pressure structural sequence, J. Appl. Phys. 113 (12) (2013) 123510, https://doi.org/10.1063/1.4798374.

[3] P. Du, J.S. Yu, Dual-enhancement of photoluminescence and cathodoluminescence in eu^{3+}-activated $srmoo_4$ phosphors by Na^+ doping, RSC Adv. 5 (74) (2015) 60121–60128, https://doi.org/10.1039/c5ra06053b.

[4] E. Çiftyürek, K. Sabolsky, E. Sabolsky, Molybdenum and tungsten oxide based gas sensors for high temperature detection of environmentally hazardous sulfur species, Sens. Actuators B 237 (2016) 262–274, https://doi.org/10.1016/j.snb.2016.06.071.

[5] R. Künzel, N.K. Umisedo, E. Okuno, E.M. Yoshimura, A.P. de Azevedo Marques, Effects of microwave-assisted hydrothermal treatment and beta particles irradiation on the thermoluminescence and optically stimulated luminescence of $SrMoO_4$ powders, Ceram. Int. 46 (10) (2020) 15018–15026, https://doi.org/10.1016/j.ceramint.2020.03.032.

[6] M. Frank, S.N. Smetanin, M. Jelínek, D. Vyhlídal, A.A. Kopalkin, V.E. Shukshin, L.I. Ivleva, P.G. Zverev, V. Kubeček, Synchronously-pumped all-solid-state SrMoO4 Raman laser generating at combined vibrational Raman modes with 26-fold pulse shortening down to 1.4 ps at 1220 nm, Opt. Laser Technol. 111 (2019) 129–133, https://doi.org/10.1016/j.optlastec.2018.09.045.

[7] Z.A. Mikhaylovskaya, E.A. Pankrushina, E.V. Komleva, A.V. Ushakov, S.V. Streltsov, I. Abrahams, S.A. Petrova, Effect of bi substitution on the cationic vacancy ordering in SrMoO4-based complex oxides: structure and properties, Mater. Sci. Eng. B 281 (2022) 115741, https://doi.org/10.1016/j.mseb.2022.115741.

[8] H. Gao, C. Yu, Y. Wang, S. Wang, H. Yang, F. Wang, S. Tang, Z. Yi, D. Li, A novel photoluminescence phenomenon in a $SrMoO_4/SrWO_4$ micro/nano heterojunction phosphors obtained by the polyacrylamide gel method combined with low temperature calcination technology, J. Lumin. 243 (2022) 118660-1–118660-11, https://doi.org/10.1016/j.jlumin.2021.118660.

[9] F. Liu, J. Wang, L. Jiang, R. You, Q. Wang, C. Wang, Z. Lin, Z. Yang, J. He, A. Liu, P. Sun, X. Yan, G. Lu, Compact and planar type rapid response ppb-level SO2 sensor based on stabilized zirconia and SrMoO4 sensing electrode, Sens. Actuators B, Chem. 307 (2020) 127655, https://doi.org/10.1016/j.snb.2020.127655.

[10] T. Basiev, A. Sobol, Y. Voronko, P. Zverev, Spontaneous Raman spectroscopy of tungstate and molybdate crystals for Raman lasers, Opt. Mater. 15 (3) (2000) 205–216, https://doi.org/10.1016/s0925-3467(00)00037-9.

[11] E.E. Dunaeva, L.I. Ivleva, M.E. Doroshenko, P.G. Zverev, V.V. Osiko, $SrMoO_4:Pr^{3+}$ single crystals: growth and properties, Dokl. Phys. 60 (3) (2015) 122–126, https://doi.org/10.1134/s102833581503009x.

[12] T. Thongtem, S. Kungwankunakorn, B. Kuntalue, A. Phuruangratc, S. Thongtem, Luminescence and absorbance of highly crystalline camoo$_4$, srmoo$_4$, cawo$_4$ and srwo$_4$ nanoparticles synthesized by co-precipitation method at room temperature, J. Alloys Compd. 506 (2010) 475–481, https://doi.org/10.1016/j.jallcom.2010.07.033.

[13] S. Swathi, R. Yuvakkumar, P.S. Kumar, G. Ravi, D. Nanthini, D. Velauthapillai, Flower like strontium molybdate for efficient energy conversion applications, Fuel 308 (2022) 122051, https://doi.org/10.1016/j.fuel.2021.122051.

[14] R.A. Sujatha, N.A.L. Flower, G. Vinitha, R. Sharath, K.M. Rahulan, Structural and non-linear optical response of Er^{3+} doped $SrMoO_4$ nanostructures, Appl. Surf. Sci. 490 (2019) 260–265, https://doi.org/10.1016/j.apsusc.2019.06.086.

[15] S. Ramarao, S.R. Kiran, V. Murthy, Structural, lattice vibrational, optical and microwave dielectric studies on ca1-sr MoO4 ceramics with scheelite structure, Mater. Res. Bull. 56 (2014) 71–79, https://doi.org/10.1016/j.materresbull.2014.04.064.

[16] S. Vidya, A. John, S. Solomon, J. Thomas, Optical and dielectric properties of srmoo4 powders prepared by the combustion synthesis method, Adv. Math. Res. 1 (3) (2012) 191–204, https://doi.org/10.12989/amr.2012.1.3.191.

[17] M. Kusuma, K. Jagannath, Solution combustion synthesis of $SrMoO_4$ nanophosphor using different molybdenum sources and study of its photocatalytic properties, Mater. Res. Express 6 (10) (2019) 1050a1, https://doi.org/10.1088/2053-1591/ab39ec.

[18] Y. Zhang, F. Yang, J. Yang, Y. Tang, P. Yuan, Synthesis of crystalline SrMoO4 nanowires from polyoxometalates, Solid State Commun. 133 (12) (2005) 759–763, https://doi.org/10.1016/j.ssc.2005.01.016.

[19] A. Chavan, A. Gawande, V. Gaikwad, G. Jain, M. Deore, Hydrothermal synthesis and luminescence properties of Dy^{3+} doped $SrMoO_4$ nano-phosphor, J. Lumin. 234 (2021) 117996, https://doi.org/10.1016/j.jlumin.2021.117996.

[20] D.F.D. Santos, L.X. Lovisa, A.A.G. Santiago, M.S. Li, E. Longo, M.R.D. Bomio, F.V. Motta, Growth mechanism and vibrational and optical properties of $SrMoO_4$: Tb^{3+}, Sm^{3+} particles: green–orange tunable color, J. Mater. Sci. 55 (20) (2020) 8610–8629, https://doi.org/10.1007/s10853-020-04623-5.

[21] S. Paradelas, R. Gonçalves, F.V. Motta, R.C. Lima, M. Li, E. Longo, A.P. de A. Marques, Effects of microwave-assisted hydrothermal treatment and of use of capping reagent on the photophysical properties of $SrMoO_4$ phosphors, J. Lumin. 192 (2017) 818–826, https://doi.org/10.1016/j.jlumin.2017.08.016.

[22] J. Sczancoski, L. Cavalcante, M. Joya, J. Varela, P. Pizani, E. Longo, Srmoo$_4$ powders processed in microwave-hydrothermal: synthesis, characterization and optical properties, Chem. Eng. J. 140 (2008) 632–637, https://doi.org/10.1016/j.cej.2008.01.015.

[23] L. Meng, K.L.B. Wang, M.G. Ma, The progress of microwave-assisted hydrothermal method in the synthesis of functional nanomaterials, Mater. Today Chem. 1–2 (2016) 63–83, https://doi.org/10.1016/j.mtchem.2016.11.003.

[24] M. Muralidharan, K. Sivaji, Vacancy induced ferromagnetism in SrWO4 and SrMoO4 nano structured compounds, in: DAE Solid State Physics Symposium 2019, AIP Publishing, 2020.

[25] D. Guo, Q. Yang, H. Hua, C. Hu, Room temperature ferromagnetism in shuttle-like $BaMoO_4$ microcrystals, J. Phys. Chem. C 118 (25) (2014) 13826–13832, https://doi.org/10.1021/jp504429g.

[26] D.D. Santos, A.A. Santiago, M.D. Teodoro, F.V. Motta, M.R. Bomio, Investigation of the photocatalytic and optical properties of the SrMoO4/g-c3n4 heterostructure

obtained via sonochemical synthesis with temperature control, J. Environ. Manag. 325 (2023) 116396, https://doi.org/10.1016/j.jenvman.2022.116396.

[27] G.-K. Choi, S.-Y. Cho, J.-S. An, K.S. Hong, Microwave dielectric properties and sintering behaviors of scheelite compound CaMoO4, J. Eur. Ceram. Soc. 26 (10–11) (2006) 2011–2015, https://doi.org/10.1016/j.jeurceramsoc.2005.09.051.

[28] S. Arai, T. Noguchi, T. Aida, A. Yoko, T. Tomai, T. Adschiri, M. Koshimizu, Y. Fujimoto, K. Asai, Development of liquid scintillators loaded with alkaline earth molybdate nanoparticles for detection of neutrinoless double-beta decay, J. Ceram. Soc. Jpn. 127 (1) (2019) 28–34, https://doi.org/10.2109/jcersj2.18146.

[29] S. Mikhrin, A. Mishin, A. Potapov, P. Rodnyi, A. Voloshinovskii, X-ray excited luminescence of some molybdates, Nucl. Instrum. Methods Phys. Res., Sect. A 486 (1–2) (2002) 295–297, https://doi.org/10.1016/S0168-9002(02)00722-2.

[30] https://doi.org/10.1016/j.optmat.2021.110971.

[31] G. Souadi, U. Kaynar, M. Oglakci, M. Sonsuz, M. Ayvacikli, M. Topaksu, A. Canimoglu, N. Can, Thermoluminescence characteristics of a novel li2moo4 phosphor: heating rate, dose response and kinetic parameters, Radiat. Phys. Chem. 194 (2022) 110025, https://doi.org/10.1016/j.radphyschem.2022.110025.

[32] F. Danevich, B. Grinyov, S. Henry, M. Kosmyna, H. Kraus, N. Krutyak, V. Kudovbenko, V. Mikhailik, L. Nagornaya, B. Nazarenko, A. Nikolaiko, O. Polischuk, V. Puzikov, A. Shekhovtsov, V. Tretyak, Y. Vostretsov, Feasibility study of PbWO4 and PbMoO4 crystal scintillators for cryogenic rare events experiments, Nucl. Instrum. Methods Phys. Res., Sect. A, Accel. Spectrom. Detect. Assoc. Equip. 622 (3) (2010) 608–613, https://doi.org/10.1016/j.nima.2010.07.060.

[33] H. Jiang, G. Rooh, H.J. Kim, H. Park, J.H. So, S. Kim, S.K. Kim, Y.D. Kim, W. Zhang, Growth and scintillation characterizations of SrMoO4 single crystals, J. Korean Phys. Soc. 63 (10) (2013) 2018–2023, https://doi.org/10.3938/jkps.63.2018.

[34] V. Mikhailik, Y. Elyashevskyi, H. Kraus, H. Kim, V. Kapustianyk, M. Panasyuk, Temperature dependence of scintillation properties of SrMoO4, Nucl. Instrum. Methods Phys. Res., Sect. A, Accel. Spectrom. Detect. Assoc. Equip. 792 (2015) 1–5, https://doi.org/10.1016/j.nima.2015.04.018.

[35] T. Yanagida, Inorganic scintillating materials and scintillation detectors, Proc. Jpn. Acad. Ser. B 94 (2) (2018) 75–97, https://doi.org/10.2183/pjab.94.007.

[36] M. Muralidharan, V. Anbarasu, A.E. Perumal, K. Sivakumar, Enhanced ferromagnetism in Cr doped SrMoO$_4$ scheelite structured compounds, J. Mater. Sci., Mater. Electron. 27 (3) (2016) 2545–2556, https://doi.org/10.1007/s10854-015-4057-1.

[37] P.D. Esquinazi, W. Hergert, M. Stiller, L. Botsch, H. Ohldag, D. Spemann, M. Hoffmann, W.A. Adeagbo, A. Chassé, S.K. Nayak, H.B. Hamed, Defect-induced magnetism in nonmagnetic oxides: basic principles, experimental evidence, and possible devices with ZnO and TiO$_2$, Phys. Status Solidi (b) 257 (7) (2020) 1900623, https://doi.org/10.1002/pssb.201900623.

[38] R. Künzel, C.M.S. Feldhaus, Y.O.F. Suzuki, F.F. Ferreira, V.G. de Paula, L.C. Courrol, N.K. Umisedo, E.M. Yoshimura, E. Okuno, A.P. de Azevedo Marques, Photoluminescence and magnetic properties of SrMoO$_4$ phosphors submitted to thermal treatment and electron irradiation, J. Magn. Magn. Mater. 562 (2022) 169761, https://doi.org/10.1016/j.jmmm.2022.169761.

[39] A.J.J. Bos, Thermoluminescence as a research tool to investigate luminescence mechanisms, Materials 10 (2017) 1357, https://doi.org/10.3390/ma10121357.

[40] S.W.S. McKeever, Thermoluminescence of Solids, Cambridge University Press, New York, 1985.

[41] M. Kowalkińska, P. Głuchowski, T. Swebocki, T. Ossowski, A. Ostrowski, W. Bednarski, J. Karczewski, A. Zielińska-Jurek, Scheelite-type wide-bandgap ABO$_4$ compounds (a = ca, sr, and ba; b = mo and w) as potential photocatalysts for water treatment, J. Phys. Chem. C 125 (46) (2021) 25497–25513, https://doi.org/10.1021/acs.jpcc.1c06481.

[42] R. Künzel, N.K. Umisedo, R.M. Latini, E.M. Yoshimura, E. Okuno, L.C. Courrol, A.P.A. Marques, Effects of beta particles irradiation and thermal treatment on the traps levels structure and luminescent properties of bamoo$_4$ phosphor, Ceram. Int. 45 (2019) 7811–7820, https://doi.org/10.1016/j.ceramint.2019.01.087.

[43] J. Mooney, P. Kambhampati, Get the basics right: Jacobian conversion of wavelength and energy scales for quantitative analysis of emission spectra, J. Phys. Chem. Lett. 4 (19) (2013) 3316–3318, https://doi.org/10.1021/jz401508t.

[44] V. Kolobanov, I. Kamenskikh, V. Mikhailin, I. Shpinkov, D. Spassky, B. Zadneprovsky, L. Potkin, G. Zimmerer, Optical and luminescent properties of anisotropic tungstate crystals, Nucl. Instrum. Methods A 486 (2002) 496–503, https://doi.org/10.1016/S0168-9002(02)00760-X.

[45] D. Wood, J. Tauc, Weak absorption tails in amorphous semiconductors, Phys. Rev. B, Condens. Matter 5 (8) (1972) 3144–3151, https://doi.org/10.1103/PhysRevB.5.3144.

[46] N.K. Umisedo, R. Künzel, E. Okuno, E.M. Yoshimura, A.L.M. Malthez, M.B. Freitas, Spectroscopy of the gamma and x ray leakage radiation from the built-in sources of a Risø TL/OSL reader, Radiat. Meas. 71 (2014) 197–200, https://doi.org/10.1016/j.radmeas.2014.02.011.

[47] G. Kitis, J.M. Gomez-Ros, J.W.N. Tuyn, Thermoluminescence glow-curve deconvolution functions for first, second and general orders of kinetics, J. Phys. D, Appl. Phys. 31 (1998) 2636–2641, https://doi.org/10.1088/0022-3727/31/19/037.

[48] D. Afouxenidis, G.S. Polymeris, N.C. Tsirliganis, G. Kitis, Computerised curve deconvolution of tl/osl curves using a popular spreadsheet program, Radiat. Prot. Dosim. 149 (4) (2012) 363–370, https://doi.org/10.1093/rpd/ncr315.

[49] H.G. Balian, N.W. Eddy, Figure-of-merit (FOM), an improved criterion over the normalized chi-squared test for assessing goodness-of-fit of gamma ray spectral peaks, Nucl. Instr. Meth. 145 (4) (1977) 389–395, https://doi.org/10.1016/0029-554X(77)90437-2.

[50] M. Mashangva, M. Singh, T. Singh, Estimation of optimal trapping parameters relevant to persistent luminescence, Indian J. Pure Appl. Phys. 49 (2011) 583–589.

[51] R. Chen, V. Pagonis, J. Lawless, Evaluated thermoluminescence trapping parameters–what do they really mean?, Radiat. Meas. 91 (2016) 21–27, https://doi.org/10.1016/j.radmeas.2016.04.006.

[52] C. Medel-Ruiz, H.L. de Guevara, J. Molina-Contreras, C. Frausto-Reyes, Fano effect in resonant Raman spectrum of CdTe, Solid State Commun. 312 (2020) 113895, https://doi.org/10.1016/j.ssc.2020.113895.

[53] R. Javed, M. Zia, S. Naz, S.O. Aisida, N. ul Ain, Q. Ao, Role of capping agents in the application of nanoparticles in biomedicine and environmental remediation: recent trends and future prospects, J. Nanobiotechnol. 18 (1) (2020), https://doi.org/10.1186/s12951-020-00704-4.

[54] D.J. Foley, S.P. Coleman, M.A. Tschopp, G.J. Tucker, Correlating deformation mechanisms with x-ray diffraction phenomena in nanocrystalline metals using atomistic simulations, Comput. Mater. Sci. 154 (2018) 178–186, https://doi.org/10.1016/j.commatsci.2018.07.056.

[55] Q. Paduano, D. Weyburne, A. Drehman, An x-ray diffraction technique for analyzing structural defects including microstrain in nitride materials, J. Cryst. Growth 318 (1) (2011) 418–422, https://doi.org/10.1016/j.jcrysgro.2010.10.019.

[56] R. Ramanan, G. Bhagavannarayana, K. Lal, Study of point defect clusters in high purity single crystals of silicon grown by Czochralski and float-zone methods by diffuse x-ray scattering technique, J. Cryst. Growth 156 (4) (1995) 377–382, https://doi.org/10.1016/0022-0248(95)00258-8.

[57] M.F.C. Abreu, F.V. Motta, R.C. Lima, M.S. Li, E. Longo, A.P. de A. Marques, Effect of process parameters on photophysical properties and barium molybdate phosphors characteristics, Ceram. Int. 40 (5) (2014) 6719–6729, https://doi.org/10.1016/j.ceramint.2013.11.134.

[58] Z. Shao, Q. Zhang, T. Liu, J. Chen, Computer study of intrinsic defects in CaWO4, Nucl. Instrum. Methods Phys. Res., Sect. B, Beam Interact. Mater. Atoms 266 (5) (2008) 797–801, https://doi.org/10.1016/j.nimb.2008.01.018.

[59] R.A. Roca, J.C. Sczancoski, I.C. Nogueira, M.T. Fabbro, H.C. Alves, L. Gracia, L.P.S. Santos, C.P. de Sousa, J. Andrés, G.E. Luz, E. Longo, L.S. Cavalcante, Facet-dependent photocatalytic and antibacterial properties of α-Ag$_2$WO$_4$ crystals: combining experimental data and theoretical insights, Catal. Sci. Technol. 5 (8) (2015) 4091–4107, https://doi.org/10.1039/c5cy00331h.

[60] A.P.A. Marques, F.V. Motta, E.R. Leite, P.S. Pizani, J.A. Varela, E. Longo, D.M.A. de Melo, Evolution of photoluminescence as a function of the structural order or disorder in CaMoO4 nanopowders, J. Appl. Phys. 104 (4) (2008) 043505, https://doi.org/10.1063/1.2968388.

[61] C.M. Sunta, Unraveling Thermoluminescence, Springer Series in Materials Science, vol. 202, Springer, India, 2015.